Heliyon 10 (2024) e27550

Contents lists available at ScienceDirect

Heliyon

journal homepage: www.cell.com/heliyon

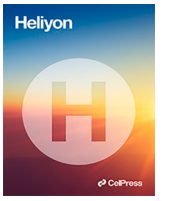

Research article

Temperature-dependent heterojunction ternary nanocomposite: Assessing photocatalytic and antibacterial applications

Alia Arif [a], Yasir Zaman [a,*], Muhammad Zahid Ishaque [a], Abu Bakar Siddique [b,**], Hira Zaman [c,***], Muhammad Shahzad [a,d], Daoud Ali [e]

[a] Department of Physics, University of Sargodha, Sargodha, 40100, Pakistan
[b] Institute of Chemistry, University of Sargodha, Sargodha, 40100, Pakistan
[c] Institute of Chemical Sciences, University of Peshawar, Khyber Pakhtunkhwa, 25120, Pakistan
[d] State Key Laboratory of Silicon Materials, Zhejiang University, Hangzhou, 310058, PR China
[e] Department of Zoology, College of Science, King Saud University, Riyadh, 11451, Saudi Arabia

ARTICLE INFO

Keywords:
Heterojunction NCPs
Hydrothermal method
Annealing temperature
Antibacterial activity
Photocatalytic activity
Degradation rate

ABSTRACT

Heterojunction nanocomposites (ZnO:NiO:CuO) were synthesized via a hydrothermal method and annealed at three different temperatures (400 °C, 600 °C, and 800 °C). The structural, optical, and electrical properties were examined by employing XRD, SEM, UV–Vis, FTIR, and LCR meter techniques to investigate the effects of annealing. Increasing the annealing temperature resulted in the nanocomposites (NCPs) exhibiting enhanced crystallinity, purity, optical properties, and improved electrical and dielectric behavior. The calculated crystalline sizes (Debye-Scherrer method) of the NCPs were determined to be 21, 26 and 34 nm for annealing temperature 400 °C, 600 °C, and 800 °C, respectively. The calculated bandgaps of synthesized samples were found in the range of 2.92-2.55 eV. This temperature-dependent annealing process notably influenced particle size, morphology, band-gap characteristics, and photocatalytic efficiency. EDX analysis affirmed the sample purity, with elemental peaks of Zn, Cu, Ni, and O. These NCPs demonstrated exceptional photocatalytic activity against various dyes solutions (Methyl orange (MO), Methylene Blue (MB), and mixed solution of dyes) under sunlight and also showed good antibacterial properties assessed by the disc diffusion method. Notably, the nanocomposite annealed at 400 °C exhibited a particularly high degradation efficiency by degrading 96% MB and 91% MO in just 90 min under sunlight.

1. Introduction

At nanoscale the characteristics of materials drastically change from their bulk equivalents, and new phenomena and applications may appear [1]. Nanotechnology is the application of nanoscience for the development of new substances, devices, and networks with unique features and abilities [2]. Nanomaterials possess unique properties due to their small size and high surface area [3]. These materials, with their small size, high surface area, and reactivity, offer a unique advantage for creating innovative substances, devices,

* Corresponding author.
** Corresponding author.
*** Corresponding author.
E-mail addresses: yasir.zaman@uos.edu.pk (Y. Zaman), abubakar.siddique@uos.edu.pk (A.B. Siddique), hzamkhan@yahoo.com (H. Zaman).

https://doi.org/10.1016/j.heliyon.2024.e27550
Received 19 December 2023; Received in revised form 15 February 2024; Accepted 1 March 2024
Available online 8 March 2024

and networks [1]. Notably, semiconductor metal oxide nanomaterials like such as TiO_2 [4], ZnO [5,6], Fe_2O_3 [7], NiO [8,9], CuO [10, 11], SnO_2 [12], CeO_2 [13] and others [14,15], demonstrated versatile properties that render them highly valuable in scientific and engineering domains. These materials, particularly notable for their potent photocatalytic capabilities, find significant applications, such as in water purification.

Metal oxide NCPs, combining various metal oxides, offer enhanced properties such as improved catalytic activity and optical characteristics, enabling applications in energy storage, sensors, biomedicine, and environmental remediation [16]. Examples include ZnO–NiO [17], ZnO–CdO [18], ZnO–MgO [19], and ZnO-$ZnWO_4$-WO_3 [20] NCPs with diverse applications. The ternary metal oxide nanocomposite ZnO–NiO–CuO [16,21], comprising ZnO, NiO, and CuO, overcomes limitations like rapid recombination and low charge generation by enhancing mechanical strength, charge separation, and photocatalytic properties. These NCPs find diverse applications in environmental remediation, antibacterial coatings, magnetic separations, and electronic devices. They exhibit promising antibacterial effects and enhanced photocatalytic degradation, attributed to the formation of heterostructures.

ZnO is classified as an n-type semiconductor with a wide bandgap energy of 3.3 eV and possesses a hexagonal structure. Notably, it is bio-safe and biocompatible, making it suitable for various biomedical applications [5,6]. NiO stands out as a p-type semiconductor with a wider bandgap energy ranging from 3.5 to 4 eV. It adopts a cubic structure and is recognized for its excellent electronic and magnetic properties, contributing to its relevance in electronic devices [8,9]. CuO is another p-type semiconductor characterized by narrow bandgap energy of 1.2 eV and a monoclinic structure. Its distinct features include high electrical conductivity and favorable optical properties, positioning it for applications in electronic and optoelectronic devices [10,11].

This paper represents as a sequel to our prior research investigating ZnO–NiO–CuO NCPs [21]. It extends our previous work by providing a comprehensive exploration of the impact of different annealing temperatures [22] on the properties of these NCPs. This paper investigates how annealing temperature influences the properties of heterojunction NCPs (ZnO:NiO:CuO) synthesized using hydrothermal methods and annealed at varied temperatures. This research is significant and novel since it seeks a complete understanding of the material properties, especially exploring the complex effects of different annealing temperatures. Examining these factors, the study aims to determine the ideal annealing temperature to modify the desired properties, such as electrical, dielectric, structural, and optical properties.

2. Experimental procedure

a. Materials and Instruments used

The raw materials for synthesis included high-purity chemicals: Zinc chloride ($ZnCl_2$), Nickel (II) nitrate hexahydrate ($Ni(NO_3)_2.6H_2O$), Copper (II) chloride dihydrate ($CuCl_2.2H_2O$), and Sodium hydroxide (NaOH) purchased from Sigma Aldrich. All solutions were prepared using distilled water, and water and ethanol were used for sample washing.

b. Instruments used

Characterization techniques included Powder XRD (PXRD) analysis with a JEOL XRD instrument using Cu-Kα lines, SEM imaging with a JEOL microscope, and UV–Visible spectrophotometry with a Shimadzu instrument for absorbance spectra in the 200–800 nm range. Electrical properties were measured using an LCR meter and Keithley I–V measurement.

2.1. Synthesis of NCPs

In this synthesis process (Fig. 1), ZnO–NiO–CuO nanoparticles (NCPs) with a 1:1:1 M ratios were prepared. Precursor salts of $ZnCl_2$ (0.6 g), $Ni(NO_3)_2.6H_2O$ (1.19 g), and $CuCl_2.2H_2O$ (0.85 g) were dissolved in 50 mL distilled water separately, to prepare 0.1 M solutions of each salt. Then, the 50 mL of each 0.1 M solution was mixed in 200 mL flask and kept on magnetic stirring for 2 h. Sodium hydroxide (NaOH) was added to maintain the pH 10 of resulting solution. The solution was stirred, heated, and then autoclaved at 150 °C for 12 h [21]. The resulting dark green solution was collected, processed, washed, dried, and annealed at 400 °C, 600 °C, and 800 °C. The resulting powder was stored in airtight jar for further applications. The representative scheme of synthesis and color of solutions are various stages are shown in Figs. 1 and 2, respectively.

Fig. 1. Schematic diagram of synthesis.

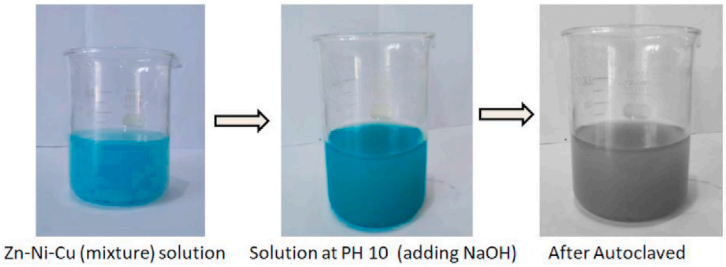

Fig. 2. Mixture solutions at different stage.

2.2. Photocatalytic degradation of dyes

The photocatalytic efficiency of ZnO–NiO–CuO NCPs was evaluated by degrading 10 ppm solutions of methylene blue (MB), methyl orange (MO), and a mixture of both dyes under sunlight. The NCPs were introduced into the dye solutions, allowed to reach equilibrium, and subsequently exposed to sunlight. Spectra were recorded at specific time intervals, revealing a gradual reduction in color over a 90-min period, indicating the degradation of dyes (Fig. 3). The absorbance data was used to determine the %degradation of dyes after regular intervals following **Equation (1)**, [21].

$$\%\ \text{degradation of dye} = \frac{C_0 - C_t}{C_0} \times 100\ \% \tag{1}$$

Where, C_o and C_t represent the initial concentration of the dye (before irradiation) and final concentration of dye after each regular interval.

2.3. Antibacterial activity

The antibacterial activity of ZnO–NiO–CuO NCPs was assessed against 2 gram-positive strains (*S. aureus* and *B. subtilis*) and 2 gram-negative strains (*E. coli* and *P. aeruginosa*) using the disc diffusion method as shown in Fig. 4 [23,24]. Firstly, bacterial colonies were grown in the freshly prepared nutrient agar solution (2g/100 mL) at 4 °C for 24 h. The turbidity of the colonies was maintained at 108 CFU (colonies forming unit) using 0.9% saline. These freshly prepared colonies were used for the seedling of cooled sterilized petri dishes containing freshly prepared agar. Petri dishes filled with agar were sterilized by autoclaving at 120 for 1 h. After seedling and solidification of agar, the NCPs were dissolved in DMSO (2 mg/5 mL) and applied to sterile paper discs, which were subsequently positioned on nutrient agar plates inoculated with bacterial cultures. Following 24 h of incubation at 37 °C, the inhibition zones were measured to assess the antibacterial efficacy of the NCPs [25].

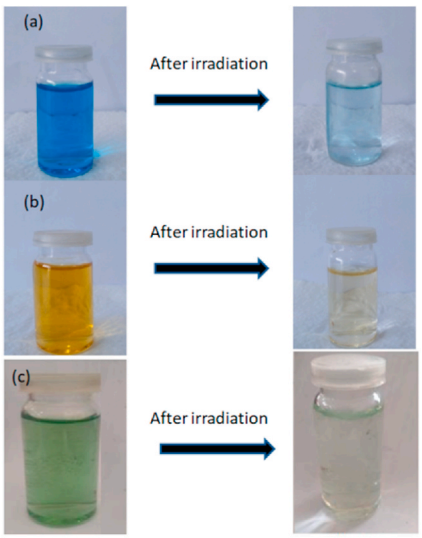

Fig. 3. Color change of the dye solution after sunlight irradiation in presence of catalyst (a) MB, (b) MO, (c) mixed solution of dyes

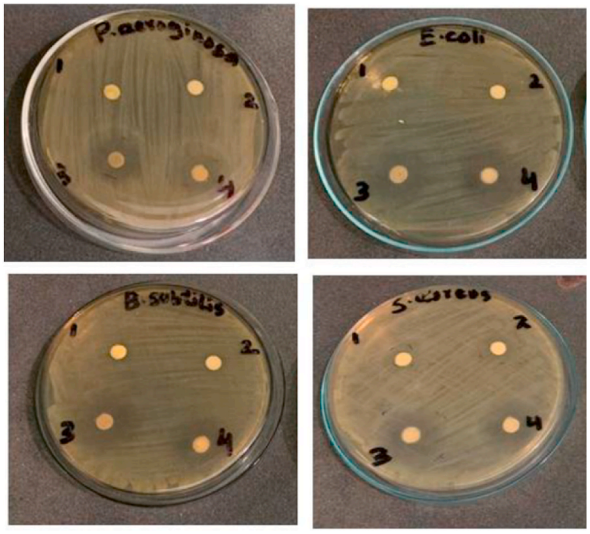

Fig. 4. Inhibition zone generated by NCP against different bacteria.

2.4. Statistical analysis

Triplicate analyses were conducted for both photocatalytic and antibacterial tests, and statistical analysis using ANOVA with significance accepted at $p < 0.05$ yielded results reported as Mean ± SD.

3. Results and discussion

3.1. XRD analysis

XRD patterns (Fig. 5) of ZnO–NiO–CuO NCPs annealed at 400 °C, 600 °C, and 800 °C (labeled ZNC-400 °C, ZNC-600 °C, and ZNC-800 °C) revealed the presence of hexagonal ZnO, cubic NiO, and monoclinic CuO phases, indicating a multiphase structure within a single matrix [16,21]. These phases were consistent with literature values. XRD analysis (Fig. 5) revealed distinct peaks corresponding to the (100), (002), (101), (102), (110), (103), (200), (112), and (201) Miller indices for ZnO (COD No. "**9004180**" [16]), the (111), (200), (220), (311), and (222) Miller indices for NiO (COD No."**01-089-3080**" [26]), and the (110), (111), (200), (−202), and (022) Miller indices for CuO (COD No "**9016105**" [16]) [21]. The absence of impurity peaks in the XRD patterns confirms the high crystallinity and purity of the ternary metal oxide ZnO–NiO–CuO NCPs. Fig. 6 shows peaks shift in annealed samples at different temperatures. The crystalline sizes of the NCPs were determined using Debye Scherrer and Williamson–Hall (W–H) method utilizing **Equations 2 and 3, respectively**.

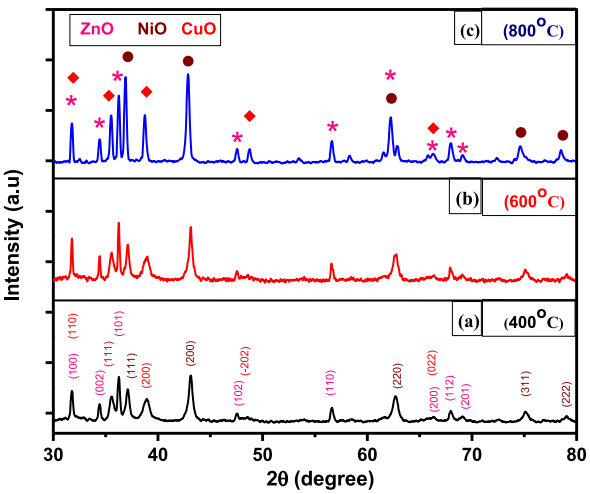

Fig. 5. XRD patterns of NCPs annealed at different temperatures.

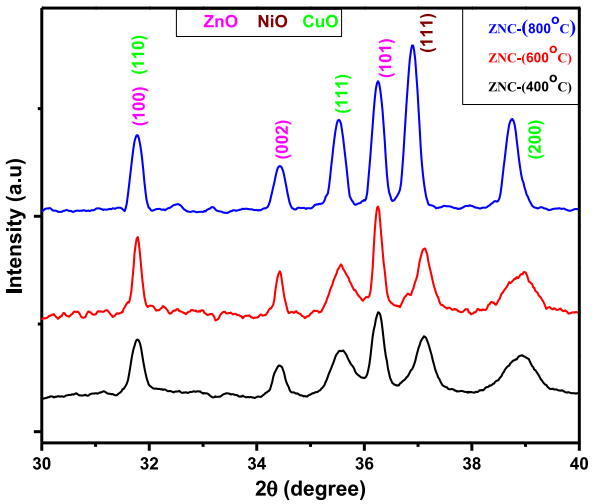

Fig. 6. Shifting of peaks in samples of annealed at different temperatures.

$$D = \frac{K\lambda}{\beta_D \cos\theta} \tag{2}$$

$$\beta_{hkl} \cos\theta = \frac{K\lambda}{D} + 4\varepsilon \sin\theta \tag{3}$$

The W–H plots of synthesized samples ZNC-400 °C, ZNC-600 °C, and ZNC-800 °C are given in Fig. 7. The measured crystalline sizes, lattice parameters, unit cell volumes, dislocation densities, lattice strains, and interplanar spacing for samples with different annealing temperature are given in Tables 1 and 2. Increasing annealing temperature resulted in sharper XRD peaks and higher intensities, indicating enhanced crystallinity of the nanoparticles [27]. Annealing at 600 °C and 800 °C caused a slight shift to lower peak angles and reduced lattice strain, with larger crystalline sizes (26.3 nm and 34.6 nm) observed due to increased atomic mobility, nucleation, and grain growth during annealing [28,29].

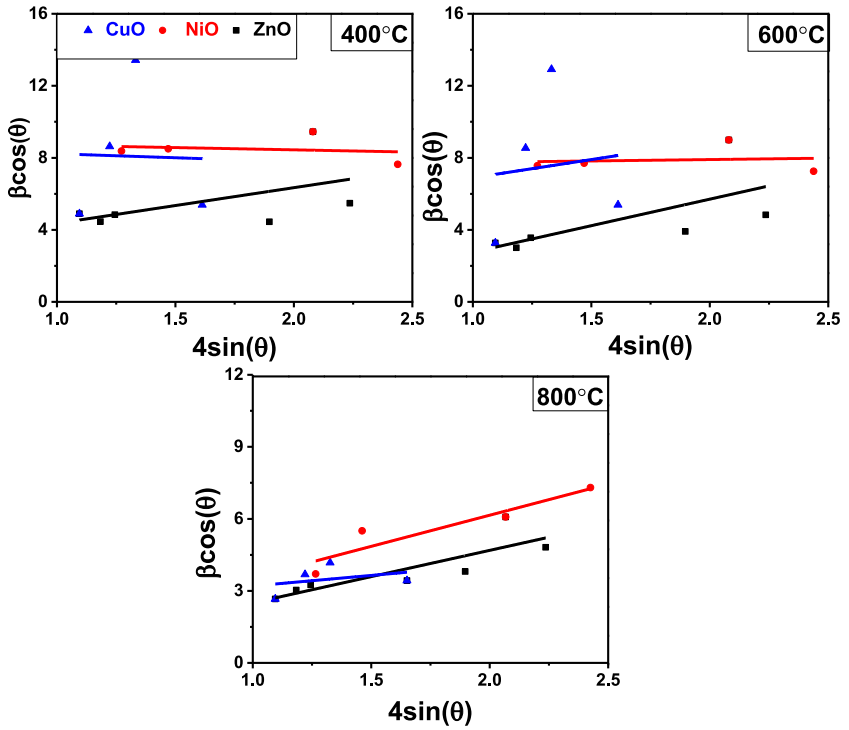

Fig. 7. Plots of W–H method for NCPs annealed at different temperature.

Table 1
Lattice parameters of samples annealed at different temperatures.

Samples oxides		a (A)	b (A)	c (A)	c/a	Volume $(A)^3$	d-spacing (A)
ZNC-400 °C	ZnO	3.24	3.24	5.19	1.60	47.40	1.89
	NiO	4.19	4.19	4.19	1.00	73.77	1.66
	CuO	4.63	3.39	5.03	1.08	78.28	2.11
ZNC-600 °C	ZnO	3.25	3.25	5.20	1.60	47.61	1.89
	NiO	4.1	4.19	4.19	1.00	73.71	1.69
	CuO	4.62	3.40	4.99	1.08	77.55	2.11
ZNC-800 °C	ZnO	3.25	3.25	5.20	1.60	47.91	1.89
	NiO	4.21	4.21	4.21	1.00	74.99	1.69
	CuO	4.64	3.42	4.94	1.06	77.62	2.38

Table 2
Different parameters of samples annealed at different temperatures.

Samples Oxides	Average crystalline size (nm)		Dislocation density $(nm)^{-2}$ $\delta \times 10^{-3}$	Lattice strain $\varepsilon \times 10^{-3}$
	Debye- Scherrer method	W.H plot Method		
ZNC-400 °C	21.51	18.88	3.13	0.91
ZnO	26.54	32.99	1.78	0.76
NiO	16.42	15.51	3.77	1.2
CuO	18.23	15.99	4.83	0.78
ZNC-600 °C	26.33	24.19	2.65	0.83
ZnO	34.52	70.01	1.31	0.66
NiO	17.72	18.26	3.24	1.21
CuO	23.09	28.46	4.34	0.72
ZNC-800 °C	34.63	85.51	1.08	0.61
ZnO	38.08	90.58	0.87	0.55
NiO	26.11	81.52	1.74	0.93
CuO	40.95	59.74	0.66	0.29

During annealing, the thermal energy increases, which results in an increase in the atomic mobility within the material. This increase in atomic mobility allows the atoms to rearrange themselves, leading to the formation of larger crystallites. The atomic diffusion rate is also increased at higher temperatures, which increases in the rate of nucleation and growth of crystallites [29]. In addition, thermal energy can help to relieve the strain on the material caused by lattice defects or structural defects. According to Table 2, the lattice strain of NCPs decreases as the annealing temperature increases. This relaxation of strain can also contribute to the growth of crystallites [30].

3.2. UV–Vis spectral analysis

UV–Vis absorption spectra (Fig. 8) of CuO–ZnO–NiO NCPs exhibited absorption maxima in the 230–330 nm range, lower than pure

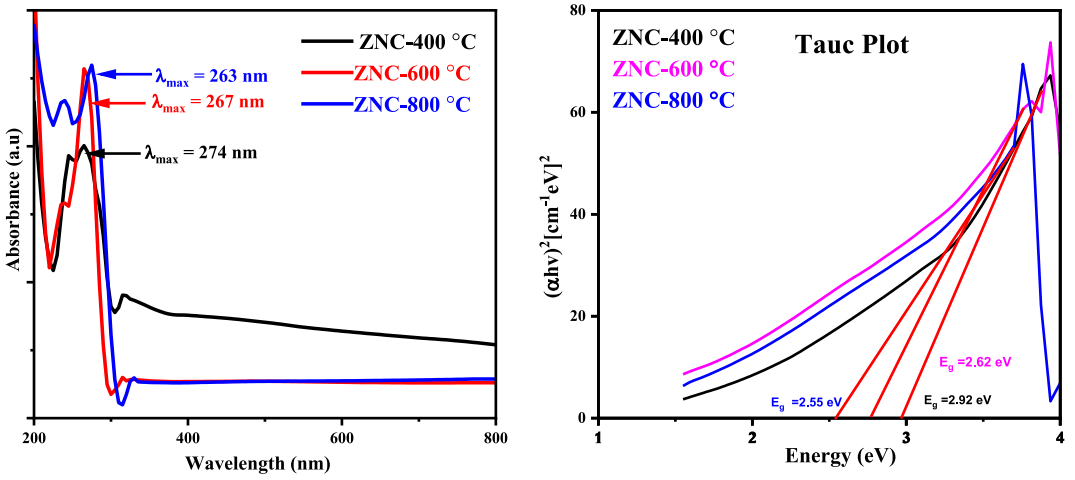

Fig. 8. UV–Vis spectra (left) and tauc plots (right) of samples annealed at different temperatures.

ZnO, CuO, and NiO NPs, indicating potential coupling effects or defect energy levels [21,31]. With increasing annealing temperature, a red shift in the absorption band edges was observed, consistent with the changes in crystallite sizes seen in XRD results. The calculated bandgap values for the NCPs annealed at 400 °C, 600 °C, and 800 °C were listed in Table 3. This reduction in bandgap with increasing annealing temperature is attributed to quantum confinement effects, which result from larger crystalline sizes in the material [32]. In nanoscale materials, increased crystalline size leads to closely spaced energy levels, causing a decrease in the bandgap energy [33].

3.3. FTIR analysis

The FTIR spectra (Fig. 9) of CuO–NiO–ZnO oxide NCPs in the range of 400–4000 cm^{-1} reveal vibrations of metal-oxygen (M − O) bonds below 1000 cm^{-1} and the presence of hydroxyl groups (O–H) in the 3570-3200 cm^{-1} region [34,35]. Increasing annealing temperature causes slight shifts in certain peaks, likely due to changes in the bonding environment, lattice vibrations, or molecular interactions [36]. Table 4 presents the measured values of effective masses, bond lengths, and force constants of ZnO, NiO, and CuO for the synthesized samples [37,38]. Higher annealing temperatures promote desorption of water molecules and hydroxyl groups from the material's surface, leading to weaker –OH stretching peaks. Stronger peaks in the fingerprint region around 480 cm^{-1} indicate enhanced atom and molecule mobility, facilitating improved bond formation and alignment, particularly in M − O bonds [39,40].

3.4. SEM & EDX analysis

SEM images (Fig. 10) of CuO–NiO–ZnO NCPs revealed irregular, mixed rod, and spherical structures, indicating compatibility between different metal oxide phases. Higher annealing temperatures (400 °C, 600 °C, and 800 °C) improved the NCPs morphology, resulting in larger particle sizes and potentially more uniform structures [41]. EDX analysis was conducted on samples synthesized at constant concentration ratios to assess both purity and composition, as illustrated in Fig. 10(d). The elemental analysis revealed distinct peaks corresponding to all elements (Zn, Cu, Ni, and O) in the EDX spectra, aligning well with the prescribed ratio of salts for each ternary metal oxide. The absence of any additional peaks affirmed the purity of samples.

3.5. DC electrical properties

The current-voltage graph slope is used for the measurement of resistance, resistivity, and conductivity. Temperature-dependent electrical conductivity and resistivity of the synthesized NCPs (400–700K) displayed (Fig. 11) expected semiconducting behavior [21,42]. With increasing temperature, the greater thermal energy promotes charge carriers from the valence band to the conduction band, augmenting the number of available charge carriers and thereby enhancing electrical conductivity [43].

Increasing the annealing temperature leads to higher electrical conductivity due to larger grain growth and fewer resistive grain boundaries. The activation energy (E_a) values, calculated from log(ρ) vs. 1000/T plots (Fig. 12), decreased with increasing annealing temperature, with values of 0.51 eV, 0.47 eV, and 0.42 eV for samples annealed at 400 °C, 600 °C, and 800 °C, respectively. This decreased activation energy indicated that higher annealing temperatures provide a more favorable environment for charge carrier movement, resulting in lower energy barriers and improved conductivity in the NCPs [44].

3.6. Dielectric properties

Fig. 13 & **14** revealed that dielectric parameters [45] such as real dielectric constant (ε_r), imaginary dielectric constant (ε_i), dielectric loss (tan δ), and impedance (Z), are higher at lower frequencies, gradually decreasing with increased frequency [21]. The dielectric properties high at low frequencies are attributed to oxygen vacancies, grain boundary defects, and low conductivity. The Maxwell-Wagner interfacial model and Koop's phenomenological hypothesis explain how conducting grains and interfaces influence dielectric behavior [46]. At low frequencies, interface accumulation leads to high dielectric constant but also higher impedance and dielectric loss due to resistance [21]. As frequency increases, reduced importance of grain boundaries and ionic displacement lag result in lower resistance, impedance, and dielectric properties.

In Fig. 13, an increase in annealing temperature from 400 °C to 800 °C leads to higher values of ε_r and ε_i. This is attributed to larger grain or particle sizes, reducing grain boundary effects and enhancing dipole moments' susceptibility to the applied electric field, resulting in improved dielectric properties. In Fig. 14, increasing annealing temperature from 400 °C to 800 °C results in higher values of both real dielectric loss and impedance due to increased grain size, enhanced polarization effects, increased resistivity, and greater charge carrier mobility [47]. Overall, annealing significantly enhances dielectric properties, especially at low frequencies [44]. The nanomaterials exhibiting high dielectric constants and dielectric losses at low frequencies have diverse applications across various fields, including electronics, energy storage, telecommunications, and sensing [48,49].

Table 3
Calculated bandgap energies of synthesized samples annealed at different temperatures.

Samples	$^{\lambda}$max (nm)	E_g (eV) using tauc plot
ZNC-400 °C	263	2.92
ZNC-600 °C	267	2.62
ZNC-800 °C	274	2.55

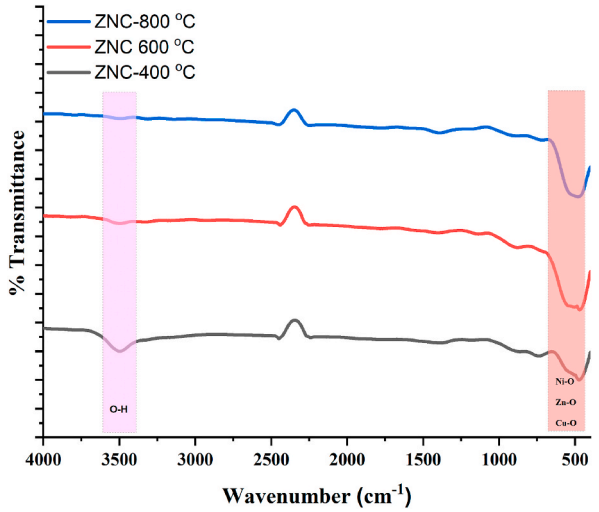

Fig. 9. FTIR spectra of samples of different annealing temperature.

Table 4
Different parameters calculated from FTIR data.

Samples	Metal- oxygen bonds	Wavenumber (cm^{-1})	Effective mass (10^{-26} kg)	Force constant (N/cm)	Bond length (A)
ZNC-400 °C	Zn–O	864	2.130	5.64	1.444
	Ni–O	737	2.083	4.08	1.608
	Cu–O	474	2.118	1.689	2.159
ZNC-600 °C	Zn–O	877	2.130	5.815	1.429
	Ni–O	648	2.080	3.104	1.762
	Cu–O	505	2.120	1.917	2.069
ZNC-800 °C	Zn–O	883	2.130	5.894	1.423
	Ni–O	717	2.080	3.801	1.647
	Cu–O	480	2.120	1.732	2.141

3.7. AC electrical conductivity

AC conductivity in ZnO–NiO–CuO NCPs increases with increasing frequency due to the activation of a hopping mechanism driven by the applied electric field, primarily attributed to the presence of mobile charge carriers [50]. At low frequencies, charge transfer is limited to neighboring lattices, but with higher frequencies, charge carriers overcome barriers, hop between localized states or defect sites, and enhance conductivity [51].

Fig. 15 demonstrates that with the increase in annealing temperature from 400 °C to 800 °C, a significant increase in AC conductivity is observed in the NCPs. Larger grain size and improved surface contact between grains result in higher conductivity, as larger grains imply fewer insulating grain boundaries [52]. This effect is consistent with XRD and SEM findings, where higher annealing temperatures lead to larger grain and crystalline sizes, promoting enhanced crystallinity for more efficient charge transport and overall increased conductivity.

4. Applications of ZnO–NiO–CuO NCPs

4.1. Photocatalytic efficacy of NCPs for dye degradation

The ZnO–NiO–CuO NCPs demonstrated superior degradation efficiency compared to individual oxides (ZnO, NiO, and CuO) due to synergistic effects. The interaction between these metal oxides improved the optical properties like light absorption, charge separation, and catalytic activity, amplifying the overall photocatalytic performance. The distinct energy levels and band structures of the individual oxides enable broader light spectrum utilization, and the heterostructure interface in the NCPs enhances charge carrier mobility, reduces recombination, and ensures long-term efficiency and stability [21].

The decrease in degradation efficiency of the ZnO–NiO–CuO NCPs for MB and MO dyes with increasing annealing temperature (from 400 °C to 800 °C) can be attributed to several factors. As the annealing temperature rises, the nanoparticles grow, resulting in larger crystalline sizes and a reduced surface area [53,54]. A larger surface area is crucial for dye adsorption and reaction rates. Furthermore, the increased annealing temperature influences the bandgap energy, leading to a decrease in bandgap due to the quantum confinement effect, affecting the NCP's optical properties [55]. The calculation of the degradation percentages of dyes

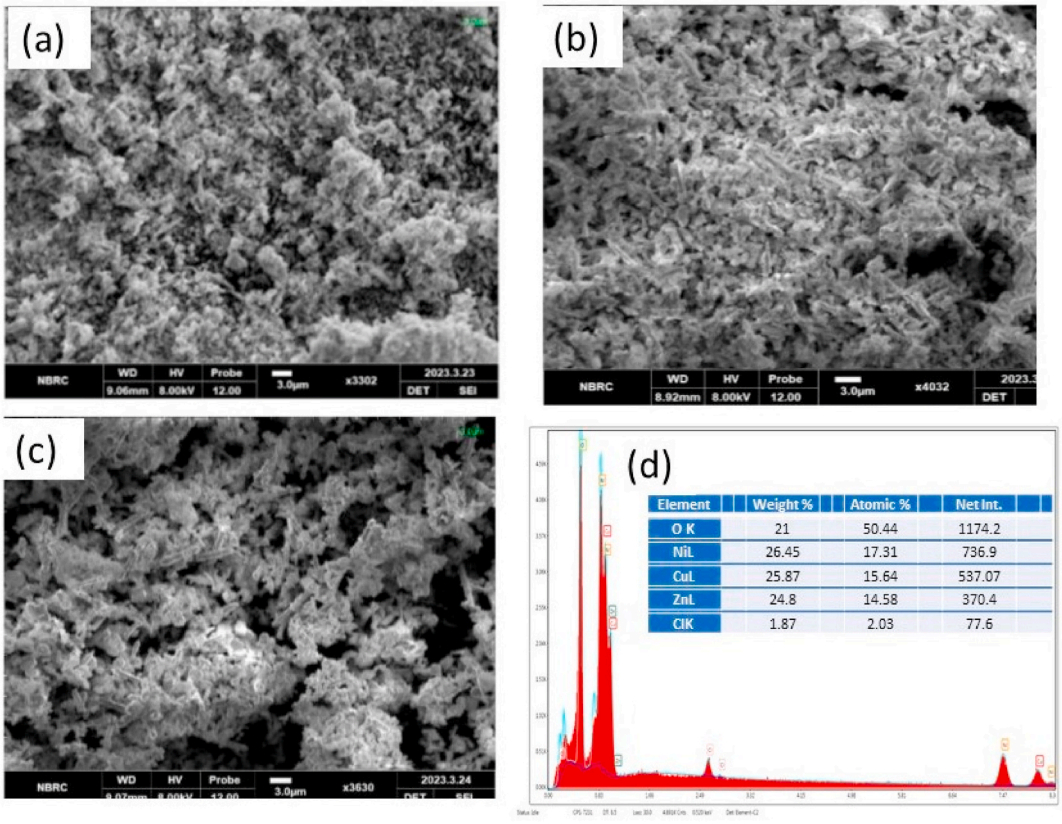

Fig. 10. SEM images of samples annealed at (a) 400 °C, (b) 600 °C, (c) 800 °C (d) EDX analysis.

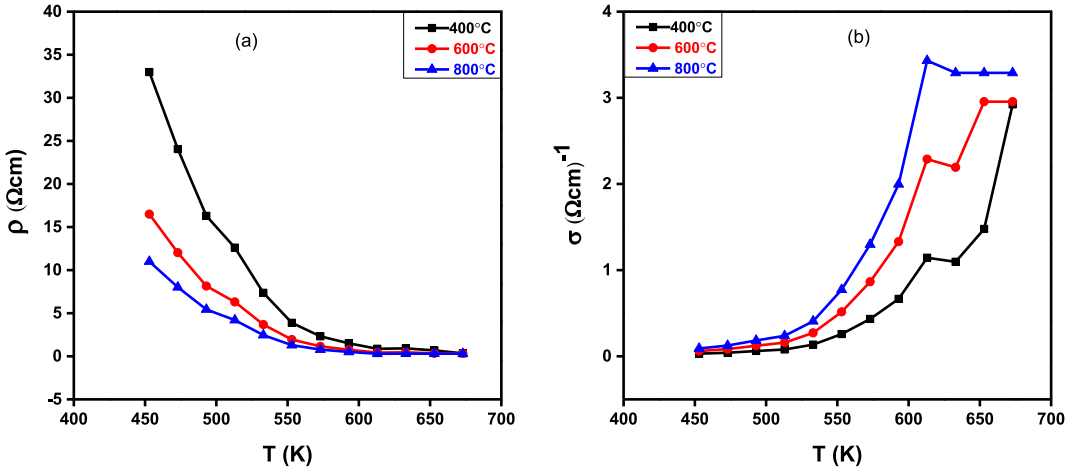

Fig. 11. Temperature-dependent (a) resistivity and (b) conductivity of samples at different annealing temperatures.

depicted in Figs. 16 and 17, as well as the determination of the reaction rate constants (k) shown in Figs. 18 and 19, is detailed in Table 5 for various samples. Studying the photocatalytic degradation of dye mixtures directly addresses the practical requirement for efficient treatment solutions in environmental applications involving polluted water bodies. The comparison of degradation efficiency of MB dye with other reported NPCs, as summarized in Table 6.

By comparison with the reported catalysts, it can be observed that the synthesized catalyst is more efficient to degrade the azo dyes in sunlight irradiation.

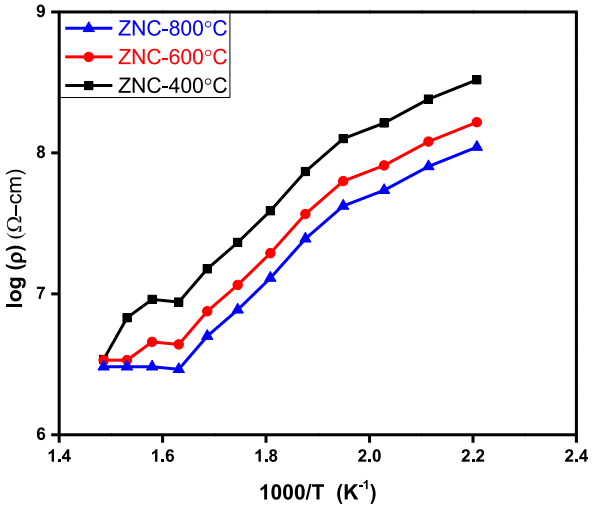

Fig. 12. Plot of log (ρ) vs 1000/T (a) for different annealing temperatures of ZnO–NiO–CuO NCPs.

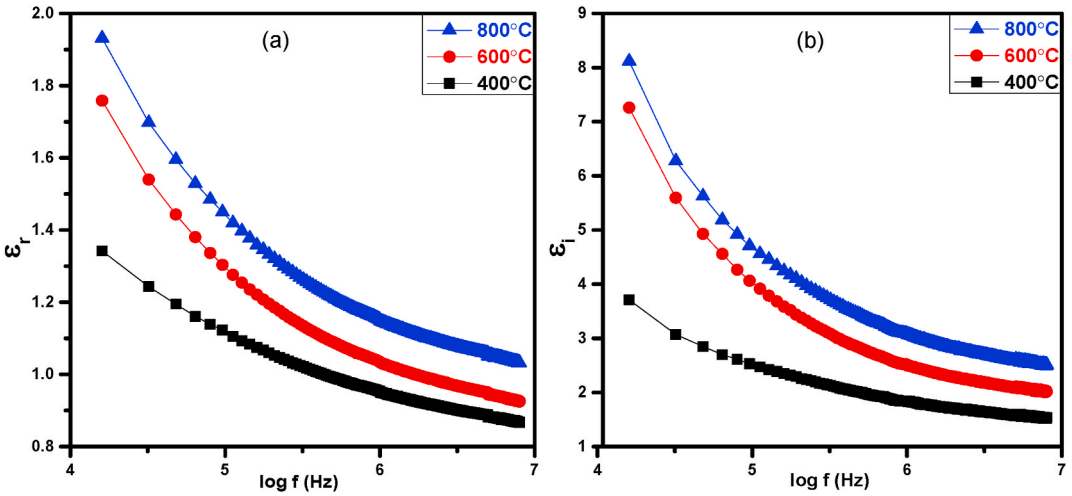

Fig. 13. Plots of NCPs at different annealing temperature (a) log(f) vs εr, and (b) log(f) vs εi.

4.1.1. Proposed mechanism

The catalytic activity in sunlight is advantageous to degrade azo dyes instead of using hazardous chemicals or high energy consumption techniques, like reverse osmosis. During sunlight exposure, the photocatalyst having appropriate bandgap absorbs light energy to generate electron-hole pairs (e^--h^+). Excited electrons in the CB reduce adsorbed pollutants, while holes in the VB oxidize them. This dual action of electron transfer and hole oxidation leads to the effective degradation of organic pollutants, transforming them into simpler and less harmful substances. Thus, photocatalysis offers a promising approach to environmental purification. Proposed mechanism of action can be illustrated by **Equations (4)–(10)**.

$$ZnO - NiO - CuO + h\nu \rightarrow ZnO - NiO - CuO\left(e^-_{CB} + h^+_{VB}\right) \quad (4)$$

$$ZnO - NiO - CuO\left(e^-_{CB}\right) + O_2 \rightarrow ZnO - NiO - CuO + O_2^* \quad (5)$$

$$H_2O \rightarrow H^+ + OH^- \quad (6)$$

$$O_2^* + H^+ \rightarrow HO_2^* \quad (7)$$

$$ZnO - NiO - CuO\left(e^-_{CB}\right) + HO_2^* + H^+ \rightarrow H_2O_2 \quad (8)$$

$$ZnO - NiO - CuO\left(h^+_{VB}\right) + \text{Dye} \rightarrow \text{Degradation product} \quad (9)$$

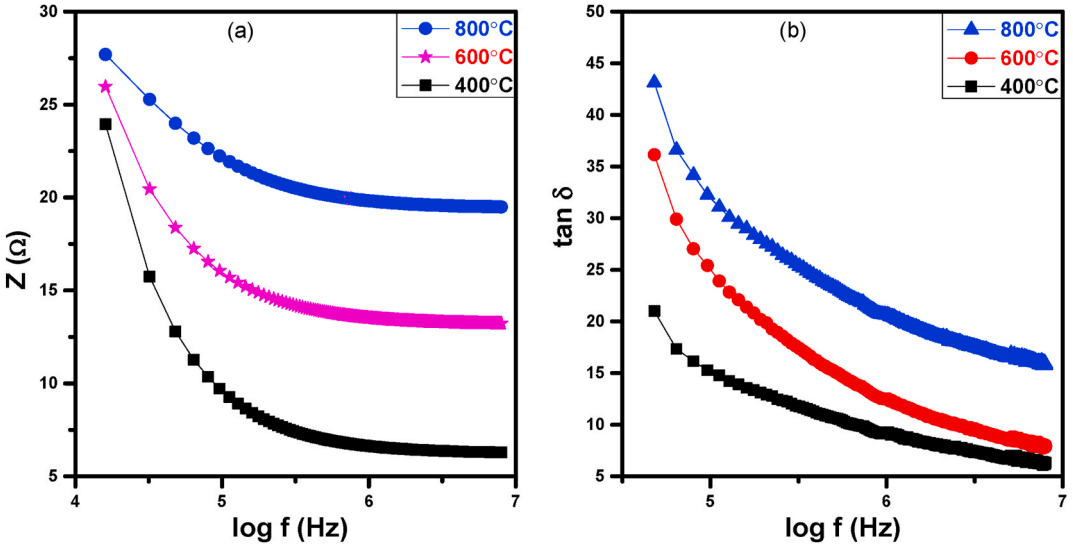

Fig. 14. Plots of NCPs at different annealing temperature (a) log f vs impedance (z), and (b) log f vs imaginary dielectric loss (tan δ).

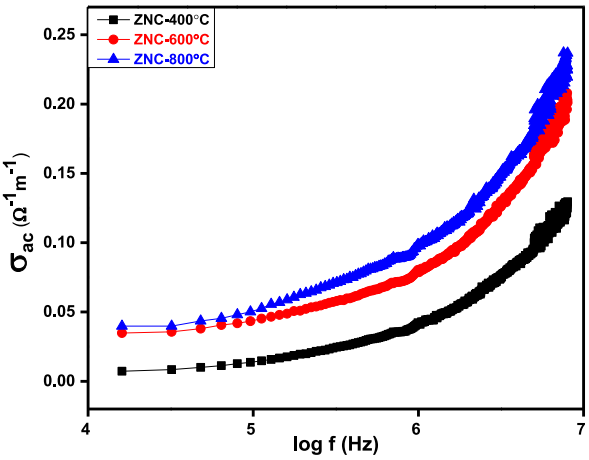

Fig. 15. Plot of log (f) vs σac (a) samples at different annealing temperature.

$$ZnO - NiO - CuO\left(e_{CB}^{-}\right) + Dye \rightarrow Degradation\ product \quad (10)$$

The pictorial representation of dye degradation mechanism is shown as in Fig. 19.

4.2. *Antibacterial activity*

The antibacterial activity of ZnO–NiO–CuO NCPs was evaluated using the disc diffusion method [56,57]. For the studies, 2 gram-positive strains (*S. aureus* and *B. subtilis*) and 2 gram-negative strains (*E. coli* and *P. aeruginosa*) of bacteria were used and results of activity are shown in Fig. 20 and Table 7. Increasing the annealing temperature of the ZnO–NiO–CuO NCPs leads to an increase in the zone of inhibition in antibacterial activity [21]. Higher annealing temperatures promote the formation of well-defined crystalline structures in the NCPs. The small crystallite size of NCPs enhances the antibacterial properties of the material, leading to a larger zone of inhibition. NCPs have the capability to interact with bacterial cells, resulting in the disruption of the cell membrane or cell wall. This interaction includes the generation of reactive oxygen species such as $^{\bullet}O_2^-$, H_2O_2, and $^{\bullet}OH$ etc., upon contact with bacteria. The ROS induce oxidative stress, leading to the impairment of bacterial DNA, proteins, and other cellular components, ultimately resulting in bacterial cell death.

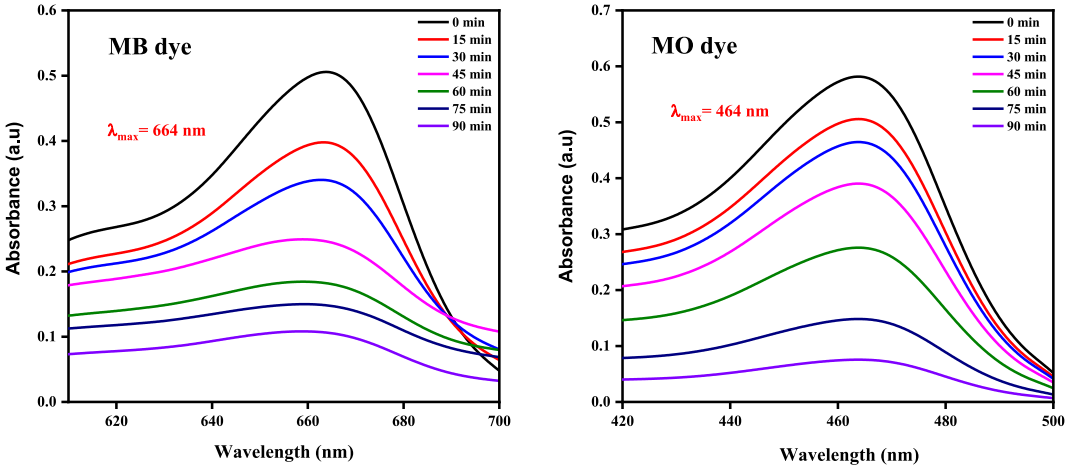

Fig. 16. Degradation efficiency vs irradiation time plots of ZnO–NiO–CuO NCPs for MB (left) and MO(right) dye.

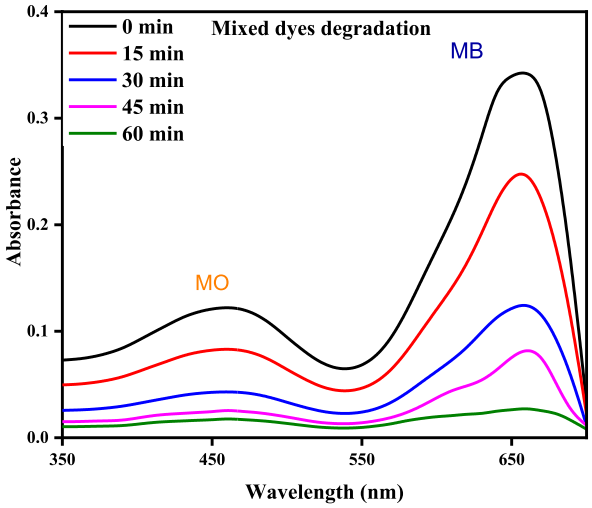

Fig. 17. Degradation efficiency vs irradiation time plots of ZnO–NiO–CuO NCPs for the mixed dyes (MO + MB).

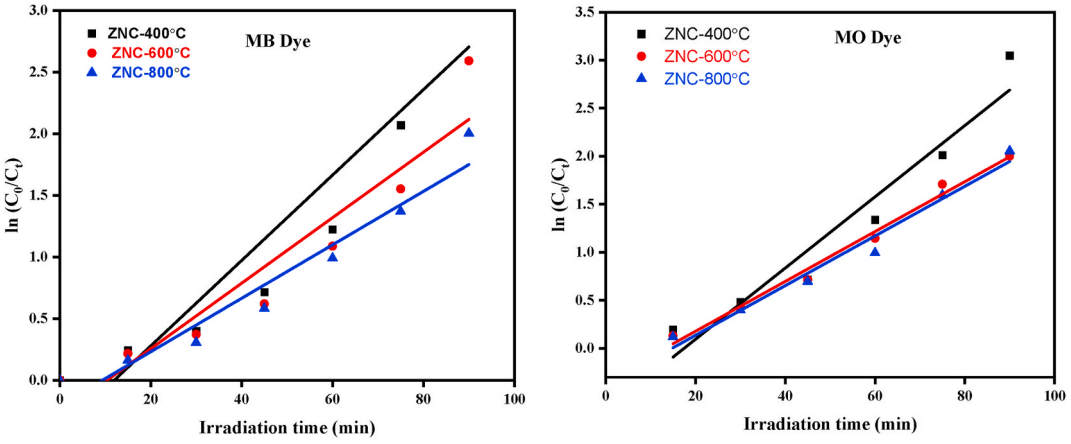

Fig. 18. $\ln(C_0/C_t)$ vs irradiation time plots of ZnO–NiO–CuO NCPs.

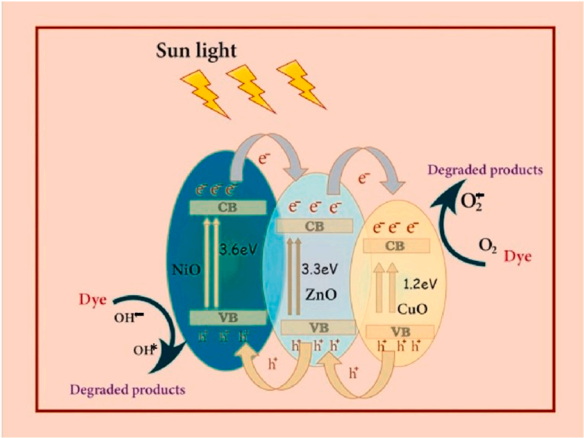

Fig. 19. Pictorial representation of dye degradation mechanism.

Table 5
Reaction rate constant (k) and degradation % of dyes for different samples.

Samples	k for MB (min^{-1})	k for MO (min^{-1})	k for MB + MO (min^{-1})	Degradation% of MB dye	Degradation% of MO dye	Degradation% of MB + MO solution
ZNC-400 °C	0.0346	0.0240	0.0301	96	91	75
ZNC-600 °C	0.0265	0.0209	0.0249	92	86	71
ZNC-800 °C	0.0216	0.0185	0.0205	86	84	64

Table 6
Comparison of degradation efficiency of various catalysts to degrade azo dyes.

Samples	Degradation efficiency (%)	References
Fe_3O_4–CuO–ZnO	79 %	[53]
ZnO/graphene/TiO_2	82 %	[54]
NiO–Fe_2O_3–CdO	85 %	[55]
CdO–NiO–ZnO	86 %	[56]
CdO–ZnO–MgO	91 %	[57]
ZnO–NiO–CuO	96 %	Present work

5. Conclusion

Increasing the annealing temperature resulted in increase of crystallite size (from 26 to 34 nm) and crystallinity, attributed to enhanced nucleation and grain growth. UV–Vis. spectra demonstrated a decrease in the bandgap of the NCPs from 2.92, 2.6 and 2.55 eV with increasing annealing temperature from 400 °C to 800 °C, attributed to the larger crystallite size. FTIR spectra of the NCPs revealed the presence of metal-oxygen and –OH molecular bonds. Increasing the annealing temperature led to weaker –OH bond peaks and stronger M − O bond signals, indicating a change in bond strengths. SEM images of the synthesized NCPs exhibited irregular mixed rod and spherical nanostructures and agglomeration occur due to increasing annealing temperature. Higher annealing temperature leads to increased electrical conductivity by promoting crystalline growth, facilitating charge carrier movement, and increasing charge carrier density within the NCPs. With increasing annealing temperatures lead to the increased dielectric constant in synthesized NCPs due to larger grain size, enhancing polarization effects, resistivity, and charge carrier mobility. Increasing annealing temperature enhances AC conductivity in NCPs by improving grain size and surface contact. The synthesized ZnO–NiO–CuO NCPs annealed at 400 °C, 600 °C, and 800 °C exhibited remarkable photocatalytic degradation efficiency (96, 92 and 86%, respectively) for MB and (91, 86 and 84%, respectively) MO, under sunlight irradiation, attributed to its heterostructure that promoted efficient charge carrier generation, stability and reduced recombination rates of charge carriers. Gram-positive and gram-negative bacterial strains were tested to examine the antibacterial activity of the ZnO–NiO–CuO NCPs. The NCPs were found more active towards the growth inhibition of gram-negative bacterial strains.

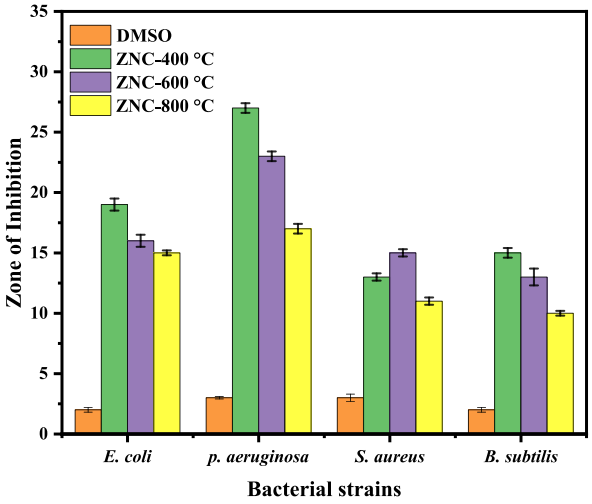

Fig. 20. Variation of ZOI for synthesized NCPs against different bacteria.

Table 7
Antibacterial activity of ZnO–NiO–CuO NCPs.

Zone of inhibition (mm)					
		Gram Negative Bacteria		Gram Positive Bacteria	
No.	Samples	*E. coli*	*P. aeruginosa*	*S. aureus*	*B. subtilis*
1	DMSO (negative control)	2	3	3	2
2	ZNC-400 °C	19	27	13	15
3	ZNC-600 °C	16	23	15	13
4	ZNC-800 °C	15	17	11	10

Data availability statement

All the data is available in the manuscript. Additional information/data can be provided on request.

CRediT authorship contribution statement

Alia Arif: Writing – original draft, Software, Formal analysis, Data curation, Conceptualization. **Yasir Zaman:** Writing – review & editing, Supervision, Funding acquisition, Formal analysis, Conceptualization. **Muhammad Zahid Ishaque:** Supervision, Project administration, Formal analysis, Conceptualization. **Abu Bakar Siddique:** Writing – review & editing, Software, Investigation, Formal analysis. **Hira Zaman:** Writing – review & editing, Software, Formal analysis, Conceptualization. **Muhammad Shahzad:** Software, Formal analysis, Data curation. **Daoud Ali:** Software, Formal analysis.

Declaration of competing interest

The authors declare no conflicts of interest.

Acknowledgment

The authors extend their appreciation to Researchers Supporting Project number (RSP2024R165), King Saud University, Riyadh, Saudi Arabia.

References

[1] G. Korotcenkov, B. Cho, Introduction to nanomaterials and nanotechnology, Chemical Sensors: Fundamentals of Sensing Materials 2 (2010) 1. Nanostructured Materials.
[2] J. Hulla, S. Sahu, A. Hayes, Nanotechnology: history and future, Hum. Exp. Toxicol. 34 (12) (2015) 1318–1321.
[3] S.V. Ganachari, et al., Synthesis Techniques for Preparation of Nanomaterials, Handbook of ecomaterials, 2017, pp. 83–103.
[4] A.J. Haider, et al., Exploring potential environmental applications of TiO2 nanoparticles, Energy Proc. 119 (2017) 332–345.
[5] M. Soosen Samuel, L. Bose, K. George, Optical properties of ZnO nanoparticles, Academic Review 16 (2009) 57–65.

[6] S. Satpathy, et al., Structural, optical, antimicrobial and ferromagnetic properties of Zn1− xLaxO nanorods synthesized by chemical route, J. Alloys Compd. 865 (2021) 158937.
[7] R. Zysler, D. Fiorani, A. Testa, Investigation of magnetic properties of interacting Fe2O3 nanoparticles, J. Magn. Magn Mater. 224 (1) (2001) 5–11.
[8] b. Anandan, V. Rajendran, Morphological and size effects of NiO nanoparticles via solvothermal process and their optical properties, Mater. Sci. Semicond. Process. 14 (1) (2011) 43–47.
[9] U. Panigrahi, et al., Zn doping induced enhancement of multifunctional properties in NiO nanoparticles, J. Alloys Compd. 833 (2020) 155050.
[10] M.E. Grigore, et al., Methods of synthesis, properties and biomedical applications of CuO nanoparticles, Pharmaceuticals 9 (4) (2016) 75.
[11] P. Mallick, S. Sahu, Structure, microstructure and optical absorption analysis of CuO nanoparticles synthesized by sol-gel route, Nanosci. Nanotechnol. 2 (3) (2012) 71–74.
[12] P. Chetri, A. Choudhury, Investigation of optical properties of SnO2 nanoparticles, Phys. E Low-dimens. Syst. Nanostruct. 47 (2013) 257–263.
[13] S. Kumar, et al., Structural and magnetic properties of Ni doped CeO2 nanoparticles, J. Nanosci. Nanotechnol. 10 (11) (2010) 7204–7207.
[14] F. Fathirad, et al., Three-layer magnetic nanocomposite containing semiconductor nanoparticles as catalyst for dye removal from water solutions under visible light, Iran. J. Chem. Chem. Eng. (Int. Engl. Ed.) 40 (6) (2021) 1749–1756.
[15] F. Ziaadini, et al., Photocatalytic degradation of methylene blue from aqueous solution using Fe3O4@ SiO2@ CeO2 core-shell magnetic nanostructure as an effective catalyst, Advances in environmental technology 5 (2) (2019) 127–132.
[16] A.O. Juma, et al., Synthesis and characterization of CuO-NiO-ZnO mixed metal oxide nanocomposite, J. Alloys Compd. 723 (2017) 866–872.
[17] A. Chrissanthopoulos, et al., Synthesis and characterization of ZnO/NiO p–n heterojunctions: ZnO nanorods grown on NiO thin film by thermal evaporation, Photon. Nanostruct: Fundam. Appl. 9 (2) (2011) 132–139.
[18] R. Saravanan, et al., ZnO/CdO composite nanorods for photocatalytic degradation of methylene blue under visible light, Mater. Chem. Phys. 125 (1–2) (2011) 277–280.
[19] P. Panchal, et al., Phytoextract mediated ZnO/MgO nanocomposites for photocatalytic and antibacterial activities, J. Photochem. Photobiol. Chem. 385 (2019) 112049.
[20] Y. Wang, et al., Structural and photoelectrocatalytic characteristic of ZnO/ZnWO4/WO3 nanocomposites with double heterojunctions, Phys. E Low-dimens. Syst. Nanostruct. 43 (1) (2010) 503–509.
[21] M.Z. Ishaque, et al., Fabrication of ternary metal oxide (ZnO: NiO: CuO) nanocomposite heterojunctions for enhanced photocatalytic and antibacterial applications, RSC Adv. 13 (44) (2023) 30838–30854.
[22] F. Fathirad, E. Sadeghi, NiFe2O4/Ti3C2 nanocomposite as an efficient catalyst for methanol electro-oxidation reaction: investigating annealing temperature and synergetic effect, Fuel 358 (2024) 130130.
[23] M. Riaz, et al., Appraisal of Antioxidant Potential and Biological Studies of Bogan Bail (Bougainvillea Glabra) Leaf Extracts Using Different Solvents, 2021.
[24] M.Z. Ishaque, et al., Photocatalytic and antibacterial potential of silver nanocubes and nanorods synthesized via polyol reduction method, Water, Air, Soil Pollut. 234 (4) (2023) 252.
[25] Y. Zaman, et al., Tamed synthesis of AgNPs for photodegradation and anti-bacterial activity: effect of size and morphology, Inorg. Chem. Commun. 150 (2023) 110523.
[26] M. Srinivasan, N. Punithavelan, Structural, morphological and dielectric investigations on NiO/CuO/ZnO combined semiconductor metal oxide structures based ternary nanocomposites, Mater. Res. Express 5 (7) (2018) 075033.
[27] T. Munawar, et al., Multi metal oxide NiO-CdO-ZnO nanocomposite–synthesis, structural, optical, electrical properties and enhanced sunlight driven photocatalytic activity, Ceram. Int. 46 (2) (2020) 2421–2437.
[28] A. Luís, et al., Influence of calcination parameters on the TiO2 photocatalytic properties, Mater. Chem. Phys. 125 (1–2) (2011) 20–25.
[29] D.K. Muthee, B.F. Dejene, Effect of annealing temperature on structural, optical, and photocatalytic properties of titanium dioxide nanoparticles, Heliyon 7 (6) (2021) 12345.
[30] M. Malek, et al., Thermal annealing-induced formation of ZnO nanoparticles: minimum strain and stress ameliorate preferred c-axis orientation and crystal-growth properties, J. Alloys Compd. 610 (2014) 575–588.
[31] E. Da'na, A. Taha, M. Hessien, Application of ZnO–NiO greenly synthesized nanocomposite adsorbent on the elimination of organic dye from aqueous solutions: kinetics and equilibrium, Ceram. Int. 47 (4) (2021) 4531–4542.
[32] S.A.-J. Jassim, E.M.A. Nassar, Effect of annealing temperature on structure and optical properties of CdO nanocrystaline thin film prepare by chemical bath deposition method, in: IOP Conference Series: Materials Science and Engineering, IOP Publishing, 2020.
[33] K. Takei, et al., Quantum confinement effects in nanoscale-thickness InAs membranes, Nano Lett. 11 (11) (2011) 5008–5012.
[34] Y. Zaman, et al., Physical properties of multifunctional TM-doped ZnO nanorods and their photocatalytic and anti-bacterial activities, Environ. Sci. Pollut. Control Ser. 30 (42) (2023) 95860–95874.
[35] M.S. Ahmad, et al., Synthesis, antioxidant activity, antimicrobial efficacy and molecular docking studies of 4-chloro-2-(1-(4-methoxyphenyl)-4, 5-diphenyl-1 H-imidazole-2-yl) phenol and its transition metal complexes, RSC Adv. 13 (14) (2023) 9222–9230.
[36] J. Kaur, et al., Raman spectra, photoluminescence and ferromagnetism of pure, Co and Fe doped SnO2 nanoparticles, Ceram. Int. 38 (7) (2012) 5563–5570.
[37] A. Ejaz, et al., Cyperus scariosus extract based greenly synthesized gold nanoparticles as colorimetric nanoprobe for Ni2+ detection and as antibacterial and photocatalytic agent, J. Mol. Liq. (2023) 123622.
[38] Y. Zaman, et al., Modified physical properties of Ni doped ZnO NPs as potential photocatalyst and antibacterial agents, Arab. J. Chem. 16 (11) (2023) 105230.
[39] O. Sneh, S.M. George, Thermal stability of hydroxyl groups on a well-defined silica surface, J. Phys. Chem. 99 (13) (1995) 4639–4647.
[40] S. Ye, et al., Facile assembled biochar-based nanocomposite with improved graphitization for efficient photocatalytic activity driven by visible light, Appl. Catal. B Environ. 250 (2019) 78–88.
[41] F.A. Akgul, et al., Influence of thermal annealing on microstructural, morphological, optical properties and surface electronic structure of copper oxide thin films, Mater. Chem. Phys. 147 (3) (2014) 987–995.
[42] M. Dinesha, et al., Temperature dependent electrical conductivity of Fe doped ZnO nanoparticles prepared by solution combustion method, J. Alloys Compd. 485 (1–2) (2009) 538–541.
[43] A. Bakri, et al., Effect of annealing temperature of titanium dioxide thin films on structural and electrical properties, in: AIP Conference Proceedings, AIP Publishing, 2017.
[44] K. Omri, I. Najeh, L. El Mir, Influence of annealing temperature on the microstructure and dielectric properties of ZnO nanoparticles, Ceram. Int. 42 (7) (2016) 8940–8948.
[45] M.M. Hassan, et al., Structural and frequency dependent dielectric properties of Fe3+ doped ZnO nanoparticles, Mater. Res. Bull. 47 (12) (2012) 3952–3958.
[46] M. Arshad, et al., Fabrication, electrical and dielectric characterization of Cd-Ni nanoferrites, Mater. Res. Bull. 87 (2017) 177–185.
[47] M. El-Desoky, et al., Effects of annealing temperatures on the structural and dielectric properties of ZnO nanoparticles, Silicon 10 (2018) 301–307.
[48] S. Chen, A. Skordos, V.K. Thakur, Functional nanocomposites for energy storage: chemistry and new horizons, Mater. Today Chem. 17 (2020) 100304.
[49] J. Azadmanjiri, et al., A review on hybrid nanolaminate materials synthesized by deposition techniques for energy storage applications, J. Mater. Chem. A 2 (11) (2014) 3695–3708.
[50] H. Bouaamlat, et al., Dielectric properties, AC conductivity, and electric modulus analysis of bulk ethylcarbazole-terphenyl, Adv. Mater. Sci. Eng. 2020 (2020) 1–8.
[51] V. Usha, et al., A study of frequency dependent electrical and dielectric properties of NiO nanoparticles, Phys. B Condens. Matter 504 (2017) 63–68.
[52] I. Kazeminezhad, A. Sadollahkhani, Influence of pH on the photocatalytic activity of ZnO nanoparticles, J. Mater. Sci. Mater. Electron. 27 (2016) 4206–4215.
[53] S.M. Mansoori, R.S. Yamgar, S.V. Rathod, Photocatalytic degradation of methylene blue dye using synthesized CuO: CdO nanocomposite, J. Sci. Res. 65 (6) (2021).

[54] A. Sadeghzadeh-Attar, Photocatalytic degradation evaluation of N-Fe codoped aligned TiO 2 nanorods based on the effect of annealing temperature, Journal of Advanced Ceramics 9 (2020) 107–122.
[55] R. Saravanan, et al., ZnO/Ag/CdO nanocomposite for visible light-induced photocatalytic degradation of industrial textile effluents, J. Colloid Interface Sci. 452 (2015) 126–133.
[56] A.B. Siddique, et al., 1,4,5-triphenyl-1H-imidazole-2-yl)phenol and its metal complexes. Synthesis, Antimicrobial Potential and Computational Studies of Crystalline 4-bromo-2-, CrystEngComm, 2022.
[57] A.B. Siddique, et al., Synthesis of hydroxyethylcellulose phthalate-modified silver nanoparticles and their multifunctional applications as an efficient antibacterial, photocatalytic and mercury-selective sensing agent, Int. J. Biol. Macromol. 256 (2024) 128009.